

Electromagnetic Scattering-Based Array Processing Methods for Near-Field Object Characterization*

Adnan Şahin and Eric L. Miller[†]
Center for Electromagnetics Research,
235 Forsyth Building, 360 Huntington Ave.
Northeastern University, Boston, MA 02115
Telephone: (617) 373-8386
Telefax : (617) 373-8627
E-mail: elmiller@cdsp.neu.edu

December 14, 1998

Abstract

We consider the use of high resolution array processing methods for detecting and localizing near-field extended targets for measurement geometries in which an array of electromagnetic receivers observes the fields scattered by the objects in response to a plane wave illumination. The algorithms presented here modify the conventional direction finding array processing techniques and use the spatial complexities of fields to determine both the range and the bearing of the targets in the region of interest. In contrast to previous source localization problems, we employ electromagnetic scattering models parameterized explicitly in terms of the target positions and which account for all multiple scattering effects.

These models play an integral role in allowing us to compute explicitly the analytical expressions for the Cramér-Rao bounds (CRB) for position estimates. The Cramér-Rao bound gives the lower bound for the estimates, and thus, specifies the lowest possible error variance that can be attained with an unbiased estimator. The theoretical Cramér-Rao bounds are then verified using Monte-Carlo simulated error variances.

Running title: EM-Based Near-Field Array Processing

*This work was supported in part DOE contract DE-FC07-95ID13395 and Army Research Office Demining MURI under Grant DAAG55-97-1-0013

[†]Communicating author

1 Introduction

Non-invasive detection and localization of objects in the near field of a receiver array have been of interest to many researchers in recent years. Some of the most promising application areas for this technology include landmine remediation, where relatively small metallic or plastic objects are located a few centimeters from the sensors, and hazardous waste remediation, where relatively large metallic objects (eg. steel metal drums) are located on the order of meters from the sensor array [1–3]. In this paper we consider a form of this problem shown in Fig. 1. A plane wave illuminates the region of interest assumed to be a homogeneous, possibly lossy medium containing one or more targets located in the near field of an array of receivers. The goal of the processing is the localization of objects with known structures.

The inherent array structure of the measurement geometry suggests that high resolution array processing techniques [4, 5] quite popular in the signal processing community would be well suited for the near-field detection problem. Typically, these techniques assume the targets are in the far field of the array so that the measured wavefronts are all planar in nature. The goal then is to determine the directions of arrival (DOA) of these wavefronts to characterize the bearing angles of the associated targets. In the case of near field target localization however, we must process scattered field data with distinctly non-planar wavefronts to determine both the range and the bearing angles of the objects. For far field range and bearing angle estimation problems, the matched field processing (MFP) approach has been successfully used for localization of typically point sources in ocean acoustics [6] and stratospherical electromagnetics [7]. MFP is an array processing technique that uses the spatial complexities of the fields to localize sources, and thus allows for estimation of both the range and the bearing of the objects.

In terms of near-field source localization, previous work has been concentrated on independently

radiating point sources [8–12] and the localization of a single extended object of unknown size and material [13]. The coherent source issue in near field localization is also dealt with in [9]. In [8,9], independent, spherical sound and noise sources are located using MUSIC based array processing methods. In [10] and [11], a similar near-field source localization scenario is considered, and performance bounds for coordinate estimates were derived for MUSIC and higher order ESPRIT based algorithms, respectively. Localization of distributed sources is reported in [14] where Valaee et al. introduced a MUSIC-based algorithm that parametrically localizes far field sources modeled with bell shaped distributions characterized by their peak position and 3 dB beamwidth. Finally, in [13] the authors employ a T-matrix type forward model as the basis for a non-linear least squares parameter estimation approach to determine the location, size, and material properties of a single object in the field of view of an array.

We present two MFP-based algorithms that localize multiple, extended scatterers placed in the near field of a receiver array. Furthermore, instead of independently radiating point sources, or sources with predetermined distribution characteristics, the radiators in this paper scatter the incident plane wave, and the physics of the multiple scattering is exactly accounted for using full scattering models. We have also determined geometries for which simpler forward scattering models can be utilized to reduce the computational complexity of the localization algorithm. At the end, we derive and verify the Cramer-Rao performance bounds for multiple, extended, near field objects.

We begin by describing a simple modification of the MUSIC algorithm in which the electromagnetic interactions between targets are ignored, and the problem is approached as if a number of spatially extended objects are independently scattering the incident electromagnetic field. While the resulting method has relatively low computational complexity, there are two issues in need of some analysis to characterize its performance. First, there is a signal coherence issue arising

from our frequency domain formulation of the problem. Second, it is necessary to determine in a quantitative manner conditions under which one may safely ignore the interactions among the scatterers. Both of these issues are addressed in Section 3.2.

In Section 3.3 we describe a second option for localizing multiple objects in which all multiple scattering effects are taken into consideration. While this approach is more computationally costly than the former, by modeling the non-trivial interactions of wavefields among scatterers, we improve our ability to resolve closely spaced scatterers. We demonstrate that this technique can easily localize the targets in geometries where the former approach fails to resolve the target positions.

Finally, we derive the Cramér-Rao bounds on variances of estimation errors for multiple object detection scenario. Our Cramér-Rao bound derivation adapts the results in [15], and accounts for near field observations. Analytical bounds of estimated object coordinates are then validated by running Monte-Carlo experiments for the estimator presented in this paper.

While our long term interests are in application of these ideas to the localization of buried objects (i.e. targets located in a halfspace), in this work, we concentrate on the simpler problem of localization when the objects are embedded in a homogeneous medium. It is our intent that the insight and experience gained from studying the homogeneous medium case will be of use when considering the more complicated half-space problem. Moreover, by considering this simpler physical problem, we are able to make extensive use of the T-matrix method [16–18] both in the localization algorithms as well as in the performance analysis. Indeed, the analytical structure of the T-matrix approach provides for the efficient computation of certain gradient information required for the method of Section 3.3 and for computing the Cramer-Rao bound in Section 4. Given the strong results in this paper, an interesting and non-trivial avenue of future research is the adaptation of the single object, half-space T-matrix approach of [19] to the multi-object

problem of interest here and the use of this forward model in an MFP-type inversion algorithm.

The remainder of the paper is organized as follows. In Section 2, we introduce the problem geometry and describe plane wave MUSIC. Section 3 is devoted to an exposition of the MFP-based algorithms. The Cramér-Rao lower bound is derived in Section 4. Numerical examples are presented in Section 5, and in Section 6, conclusions will be drawn.

2 Background

The measurement scheme depicted in Fig. 1 is considered in this paper. The objects are located in a background for which the constant electrical characteristics (relative permittivity and conductivity) are assumed known. A transverse magnetic (TM) polarized plane wave, $E_i(\mathbf{r})$, impinges on the objects, inducing surface and volume currents which in turn radiate a scattered field, $E_s(\mathbf{r})$ ¹. In this work, we are interested only in the object localization problem, thus material properties, shapes and the number of objects are assumed known.

The scattered electric field from N objects is spatially sampled by a uniformly spaced, linear array with M isotropic receivers, $M > N$. When the multiple scattering effects are taken into consideration, the measured data at the sensor outputs can be written as:

$$\mathbf{y} = \mathbf{A}_{ms}\mathbf{x} + \mathbf{n}, \quad (1)$$

where $\mathbf{A}_{ms} = [\mathbf{E}_{s1}(\mathbf{r}_1, \dots, \mathbf{r}_N) \ \mathbf{E}_{s2}(\mathbf{r}_1, \dots, \mathbf{r}_N) \ \dots \ \mathbf{E}_{sN}(\mathbf{r}_1, \dots, \mathbf{r}_N)]$ and $\mathbf{E}_{si}(\mathbf{r}_1, \dots, \mathbf{r}_N)$ denotes the scattered field observed at the array due to the i th object, in the presence of all other $(N - 1)$ scatterers, $i = 1, 2, \dots, N$. For time domain applications, the vector \mathbf{x} contains the narrow band time variations. Since we do our analysis in the frequency domain and suppress $e^{j\omega t}$, $\mathbf{x} = [1 \ 1 \ \dots \ 1]^T$. The i th column of matrix \mathbf{A}_{ms} depends not only on the position of the i th object, but also that of $(N - 1)$ other objects. Therefore, we may replace $\mathbf{A}_{ms}\mathbf{x}$ in (1) with $M \times 1$ vector

¹All analysis is in the frequency domain, thus the $e^{j\omega t}$ time dependence will be dropped.

$\mathbf{B} = \mathbf{E}_s(\mathbf{r}_1, \mathbf{r}_2 \cdots \mathbf{r}_N) = \mathbf{E}_{s1}(\mathbf{r}_1, \dots, \mathbf{r}_N) + \mathbf{E}_{s2}(\mathbf{r}_1, \dots, \mathbf{r}_N) + \dots + \mathbf{E}_{sN}(\mathbf{r}_1, \dots, \mathbf{r}_N)$, which denotes the total scattered field at the receiver array.

The recursive T matrix algorithm [16–18] is used to calculate the exact scattered field \mathbf{E}_{si} due to the i th object in the presence of other objects. The algorithm reported in [18] is designed for the efficient solution of near field scattering problems with heterogeneous collection of metallic and dielectric objects. In addition, using the recursive T-matrix algorithm the solution to the scattering problem can be written in a closed form. This property is especially useful in obtaining analytical expressions for gradients and derivatives in multi-dimensional parameter search in Section 3.3 and in Cramér-Rao bound analysis in Section 4.

Electromagnetic interactions between the objects may be ignored in favor of reducing the computational complexity of the localization process. For the method presented in Section 3.2, we use the same data model as in (1), except that the matrix \mathbf{A}_{ms} is replaced by

$$\mathbf{A}_{ss} = [\mathbf{E}_s(\mathbf{r}_1) \ \mathbf{E}_s(\mathbf{r}_2) \cdots \mathbf{E}_s(\mathbf{r}_N)]. \quad (2)$$

The $M \times 1$ vector $\mathbf{E}_s(\mathbf{r}_i)$ denotes the scattered field due to a single object located at \mathbf{r}_i , $i = 1, 2, \dots, N$, and it is calculated using the Mie series [20]. Therefore, each column of \mathbf{A}_{ss} contains the scattered field that is a function of position of only one particular object. In fact, in this definition of matrix \mathbf{A}_{ss} , each column is equivalent to those of \mathbf{A}_{ms} in (1) when all other scatterers are infinitely far away. The vector \mathbf{x} is the same as before, $\mathbf{x} = [1 \ 1 \cdots 1]^T$.

2.1 Review of Plane wave MUSIC

For plane wave MUSIC, the data model is in the following form:

$$\mathbf{y} = \mathbf{A}_{pw}\mathbf{x} + \mathbf{n}, \quad (3)$$

where $\mathbf{A}_{pw} = [\mathbf{a}(\theta_1) \ \mathbf{a}(\theta_2) \ \cdots \ \mathbf{a}(\theta_N)]$, and $\mathbf{a}(\theta_i) = [1 \ e^{jkd \cos \theta_i} \ e^{j2kd \cos \theta_i} \ \cdots \ e^{j(M-1)kd \cos \theta_i}]^T$.

Here $\mathbf{a}(\theta_i)$ is known as the direction vector, θ_i is the direction of arrival (DOA) of the i th plane

wave, k is the wave number in the medium of propagation, and d is the distance between two sensors. The experiment as represented by the data model in (3) is repeated many times in order to determine the statistics of \mathbf{y} . In particular, if L experiments are performed, then the maximum likelihood estimate of the spatial autocovariance matrix $\mathbf{R} = E\{\mathbf{y}\mathbf{y}^H\}$ is given by [4]:

$$\hat{\mathbf{R}} = \frac{1}{L} \sum_{l=1}^L \mathbf{y}_l \mathbf{y}_l^H \quad (4)$$

where \mathbf{y}_l is the data measured at the l th experiment, and superscript H denotes the complex conjugate transpose. The sample covariance matrix $\hat{\mathbf{R}}$ is used in MUSIC algorithm to separate signal and noise subspaces through the eigenspace decomposition [4]:

$$\hat{\mathbf{R}} = \hat{\mathbf{U}}_s \hat{\Lambda}_s \hat{\mathbf{U}}_s^H + \hat{\mathbf{U}}_n [\hat{\sigma}^2 \mathbf{I}] \hat{\mathbf{U}}_n^H \quad (5)$$

where $\hat{\mathbf{U}}_s$ is the estimated signal subspace matrix and contains the N signal eigenvectors, and $\hat{\mathbf{U}}_n$ is the estimated noise subspace matrix and contains $M - N$ noise eigenvectors of multiple noise eigenvalue $\hat{\sigma}^2$. The projection operator onto the noise subspace is defined as [4]:

$$\hat{\Pi}_n = \hat{\mathbf{U}}_n \hat{\mathbf{U}}_n^H. \quad (6)$$

The basic idea behind the planewave MUSIC algorithm is that the reciprocal of the “distance” between the estimated noise subspace and the true noise subspace has sharp peaks around the DOAs. Thus, if one plots this quantity versus all possible angles, estimates of DOAs can be determined by the maxima of the angular spectrum. The spatial spectrum of the MUSIC algorithm is given by [4]:

$$P_{MUSIC}(\theta) = \frac{\mathbf{a}(\theta)^H \mathbf{a}(\theta)}{\mathbf{a}(\theta)^H \hat{\Pi}_n \mathbf{a}(\theta)} \quad (7)$$

where $\mathbf{a}(\theta) = [1 \quad e^{jkd \cos \theta} \quad e^{j2kd \cos \theta} \dots e^{j(M-1)kd \cos \theta}]^T$ is the direction vector that accounts for a plane wave impinging on the array from the direction θ .

It is important to realize that the formulation of the array processing problem presented in this section implicitly assumes that the radiator is infinitely distant so that the scattered field has planar wavefronts at the sensor array. Thus, the elements of the direction vector $\mathbf{a}(\theta)$ are complex

exponentials indicative of plane wave signals. However in many applications, including near field object detection, the receivers are in the near-field region of the radiating sources, resulting in non-planar wavefronts. The target localization problem, therefore, not only requires the DOA relative to the array but also the range of the target from a point on the array.

3 Matched Field Processing for Object Localization

As mentioned in the introduction, matched field processing [6] uses the spatial complexities of the fields to localize sources in underwater acoustics. In a similar manner, plane wave MUSIC outlined in Section 2 can be modified so that the direction vector is filled with the type of the wavefront impinging on the array [2, 3, 8–10]. We divided this section into three parts. In the first part we will describe the single object localization. Even though single object localization is a subset of multiple object localization, we present it separately in order to explain the multiple object case clearly. The second part will deal with multiple objects, but the electromagnetic interaction between objects will be ignored. In the last part, we will treat multiple object detection problem when the multiple scattering effects are taken into account.

3.1 Single Object Localization

By using the spatial distribution of the scattered field, we can fill the direction vector in plane wave MUSIC with non-planar scattered fields to locate the near field objects. By modifying the spatial MUSIC spectrum in (7), we form the following spectrum:

$$P_{MUSIC}(r, \theta) = \frac{\mathbf{E}_s(r, \theta)^H \mathbf{E}_s(r, \theta)}{\mathbf{E}_s(r, \theta)^H \hat{\Pi}_n \mathbf{E}_s(r, \theta)} \quad (8)$$

where the new “direction” vector (actually, the *locus vector* in r and θ space) $\mathbf{E}_s(r, \theta)$ is now filled with the scattered field observed for an object located at $\mathbf{r} = (r, \theta)$. Then, the location $(\hat{r}, \hat{\theta})$ maximizing the MUSIC spectrum in (8) is selected as the estimated object center.

Because a two dimensional search requires that the exact scattered field be calculated at each point of the parameter mesh, this technique is in general computationally intensive. When the objects to be detected are modeled as simple shapes, computing the exact scattered field can be relatively simple. Here we consider the case of infinitely long cylinders so that the scattered field due to a plane wave can be calculated using the Mie series:

$$E_s(\rho, \phi) = \sum_{n=-\infty}^{\infty} c_n H_n^{(2)}(k\rho) e^{jn(\phi + \pi - \phi_{inc})} \quad (9)$$

where $H_n^{(2)}(.)$ is the Hankel function of the second kind of order n representing cylindrical outgoing waves, k is the wavenumber in the homogeneous, possibly lossy, background, and ϕ_{inc} is the incidence angle of the plane wave. The coefficients c_n are determined from the boundary conditions when ρ is equal to the radius of the cylinder. For computer implementations, the infinite sum in (9) is truncated at a finite value beyond which the coefficients c_n are below machine precision. Here ρ and ϕ denote the coordinates of the receivers since (9) assumes that the center of the cylinder is located at the origin. In implementing (8), translations from object-to-receiver coordinate system (ρ, ϕ) to array-to-object-position coordinate system (r, θ) are required. These translations do not significantly alter the computational load or functional form implied by (9).

Fig. 2(b) shows the MUSIC spectrum for a localization scenario when a small metallic object in 7.5 cm diameter is placed 15 cm below the array as depicted in Fig. 2(a). The 33-element linear, uniform receiver array spans an aperture of 1.5 meters. All sensors are assumed to be ideal, isotropic receivers. The operating frequency is 1.0 GHz and the plane wave is incident with 90 degrees. The lossy, homogeneous background has the same electrical characteristics of 5% moist San Antonio clay loam or 10% moist Puerto Rico clay loam ($\epsilon_b = 6\epsilon_0$, $\sigma_b = 5 \times 10^{-2} S/m$) at around 1.0 GHz [21]. The signal to noise ratio (SNR) is fixed at 0 decibels. As Fig. 2(b) depicts, the location of the object ($r = 15cm$, $\theta = 90^\circ$) is indicated with a very sharp peak. We note that

the prominent peak structure of the spectrum in this example is representative of a wide range of other cases for which the background electrical properties, target electrical characteristics and the signal to noise ratios are varied [2].

3.2 Multiple Object Localization: No Interaction

In this section, we describe multiple object localization assuming that the objects are located sufficiently far apart, so that the interactions among them can be ignored. For this case, multiple object localization is equivalent to having a superposition of cylindrical waves of the form in (9) incident on the array. Since the interactions are ignored, the scattered field due to one object is independent of the positions of the other objects, and thus we can use the single object localization approach described in previous section to search for multiple peaks in MUSIC spectrum given in (8) to determine positions of multiple objects. As in Section 3.1, the scattered field due to a single scatterer is calculated using the Mie series in (9), and a two-dimensional search is carried out to find N peaks corresponding to estimated target locations $(\hat{r}_1, \hat{\theta}_1), (\hat{r}_2, \hat{\theta}_2), \dots, (\hat{r}_N, \hat{\theta}_N)$.

The use of MUSIC in this manner raises two issues which are considered in the following paragraphs. First, because we are operating in the frequency domain, there are signal coherence difficulties which we address through the use of frequency diversity. The second issue is the need to develop a quantitative means of understanding the circumstances under which the no-interaction approximation is valid. In analyzing both of these issues, we present closed form analytical results valid for near field objects of infinitesimal radius and verify through numerical calculation that the insight provided by these expressions carries over for objects of finite size.

Because of the structure of \mathbf{x} in (1), the rank of $\mathbf{P} = E\{\mathbf{x}\mathbf{x}^H\}$, is one and so is the rank of \mathbf{R} . Thus, the signals impinging on the array are coherent. To increase the rank of \mathbf{R} (i.e. to decorrelate the signals) we repeat the scattering experiment as represented by (1) at N different frequencies

where N is the number of objects whose locations are to be determined. Thus (4) becomes:

$$\hat{\mathbf{R}}_i = \frac{1}{L} \sum_{l=1}^L \mathbf{y}_{li} \mathbf{y}_{li}^H \quad (10)$$

where \mathbf{y}_{li} is the l th data vector observed at the i th operating frequency, f_i , and $\hat{\mathbf{R}}_i$ is the spatial autocovariance matrix at f_i , $i = 1, 2, \dots, N$. Then, the rank enhanced autocovariance matrix $\hat{\mathbf{R}}_d$ is obtained by

$$\hat{\mathbf{R}}_d = \frac{1}{N} \sum_{i=1}^N \hat{\mathbf{R}}_i. \quad (11)$$

In Appendix A, we prove for $N = 2$ that in the limiting case of infinitesimal object radius, frequency diversity does, in fact, increase the rank of the autocovariance matrix $\hat{\mathbf{R}}_d$ to two. In addition, for objects with finite radii, we can computationally demonstrate that using frequency diversity we obtain a full rank autocovariance matrix. Having decorrelated the signals, the projector onto the noise subspace, $\hat{\Pi}_n$ in (8), is found from eigendecomposition of $\hat{\mathbf{R}}_d$.

While neglecting the interactions reduces the computational demand of localization considerably, it may introduce large estimation errors if the interactions are in fact sizeable. To analyze this issue we consider a scenario in which two objects are located a fixed distance beneath a receiver array and separated by a distance d .² We define the following normalized interaction term to measure the relative import of the multiple scattering between the two objects

$$\delta(d) = \frac{\|\mathbf{E}_{s1}^{(2)} - \mathbf{E}_{s1}\|_2^2}{\max_{d \in [d_{min}, d_{max}]} \|\mathbf{E}_{s1}^{(2)} - \mathbf{E}_{s1}\|_2^2} \quad (12)$$

where $\mathbf{E}_{s1}^{(2)}$ is the scattered field vector observed at the array due to the first object in the presence of the second object, \mathbf{E}_{s1} is the scattered field from the first object when there are no other scatterers, and d_{min} and d_{max} are limits over which we want to perform the analysis as dictated by the nature of the underlying application. In Appendix B we provide a closed form expression for δ in the case of two infinitesimally thin scatterers and show in Section 5.1, that (a) the δ for filamentary

²While not the most general setup, this configuration is representative of the types of application of interest in this paper (eg. mine detection) in which at most a couple of objects are in the array's field of view at about the same depth. Moreover, this simplified problem provides insight which may well be of use in more complex situations.

objects bounds those for the extended objects for a wide range of distances and (b) the error in the localization procedure tracks closely the value of δ . Thus, the expression in Appendix B can be used to determine the degree of interaction between two scatterers in terms of spacing and electrical properties of medium of propagation. By selecting a desired interaction level, we may calculate the minimum distance between scatterers that satisfy this a priori level. If for a given scenario we suspect that the actual distance is smaller than the minimum distance, then we should not ignore the interactions, and use the technique in Section 3.3 to localize the objects.

3.3 Multiple Object Localization: With Interaction

In this section, we describe multiple object localization using MUSIC when the electromagnetic interactions between objects are completely taken into consideration. In a sense, this is the multi-dimensional equivalent of single object detection where we aggregate all scatterers into one, large scatterer whose electrical characteristics are defined by the $2N$ co-ordinates of the individual objects. For object localization, then, we form the following MUSIC spectrum:

$$P_{MUSIC}(r_1, \theta_1, r_2, \theta_2, \dots, r_N, \theta_N) = \frac{\mathbf{E}_s(\mathbf{r}_1, \mathbf{r}_2, \dots, \mathbf{r}_N)^H \mathbf{E}_s(\mathbf{r}_1, \mathbf{r}_2, \dots, \mathbf{r}_N)}{\mathbf{E}_s(\mathbf{r}_1, \mathbf{r}_2, \dots, \mathbf{r}_N)^H \hat{\Pi}_n \mathbf{E}_s(\mathbf{r}_1, \mathbf{r}_2, \dots, \mathbf{r}_N)} \quad (13)$$

where $\mathbf{E}_s(\mathbf{r}_1, \mathbf{r}_2, \dots, \mathbf{r}_N)$ denotes the total scattered field due to objects located at $\mathbf{r}_i, i = 1, 2, \dots, N$ and is filled using the recursive T-matrix algorithm [16–18]. In order to find the positions of the objects, then, we perform a $2N$ -dimensional search in location space of all objects, $(r_1, \theta_1), (r_2, \theta_2), \dots, (r_N, \theta_N)$. The coordinates $(\hat{r}_1, \hat{\theta}_1), (\hat{r}_2, \hat{\theta}_2), \dots, (\hat{r}_N, \hat{\theta}_N)$ at which the spectrum (13) reaches maximum give us the estimated target locations. Finally we note that since there is only a single signal vector defined by the position of all the objects, we have no signal coherence issue here.

The computational complexity of this approach is considerably larger than the no interaction case for two inter-related reasons: the repeated use of the forward scattering model many times for the $2N$ -dimensional search, and the extra cost of taking electromagnetic interactions into account

in the exact forward model. To keep the computational load at reasonable levels, we used the recursive T-matrix algorithm given in [18] to calculate the scattered fields due to multiple objects. This variant of T matrix algorithm is specifically designed for the efficient solution of near field scattering problems involving heterogeneous collections of metallic and dielectric objects. Finally, to further reduce the computational load, we employ a variable step-size steepest ascent approach to maximize (13) which, for the problems of interest here typically converges to the neighborhood of the maximum in 7-10 iterations after which point we use a less costly simplex search [22] to locate the exact maximum. Explicit, closed form expressions for the gradient of the MUSIC spectrum with respect to the target coordinates are provided through the use of the T matrix forward model. The associated long and tedious formulae are provided in [23].

4 Cramér-Rao Performance Bounds on Object Localization

The Cramer-Rao Bound (CRB) provides very valuable information about the lower limit for the variance of any unbiased estimator. In order to find CRB, however, one should have a closed form expression of the log-likelihood function. In this section, we will extend the results in [15] to find the Cramér-Rao bounds for the near field, multiple object detection geometries. Since the additive noise in (1) is white and Gaussian, the log-likelihood function can be written as [15]:

$$\ln \mathcal{L} = \text{constant} - 2ML \ln \sigma - \frac{1}{\sigma^2} \sum_{l=1}^L [\mathbf{y} - \mathbf{A}_{ms} \mathbf{x}]^H [\mathbf{y} - \mathbf{A}_{ms} \mathbf{x}] \quad (14)$$

where σ^2 is the noise variance, M is the number of receivers and L is the number of data vectors used for estimating the covariance matrix $\hat{\mathbf{R}}$ in (4).

Given the log-likelihood function, the Fisher Information Matrix (FIM) can be written as:

$$\mathbf{J} = E\{\psi\psi^T\} \quad (15)$$

where $\psi = [\frac{\partial \ln \mathcal{L}}{\partial r_1} \frac{\partial \ln \mathcal{L}}{\partial \theta_1} \dots \frac{\partial \ln \mathcal{L}}{\partial r_N} \frac{\partial \ln \mathcal{L}}{\partial \theta_N}]^T$. The FIM is then expressed in matrix form as:

$$J = \begin{bmatrix} \Gamma_{r_1 r_1} & \Gamma_{r_1 \theta_1} & \cdots & \Gamma_{r_1 r_N} & \Gamma_{r_1 \theta_N} \\ \Gamma_{\theta_1 r_1} & \Gamma_{\theta_1 \theta_1} & \cdots & \Gamma_{\theta_1 r_N} & \Gamma_{\theta_1 \theta_N} \\ \vdots & \vdots & \ddots & \vdots & \vdots \\ \Gamma_{r_N r_1} & \Gamma_{r_N \theta_1} & \cdots & \Gamma_{r_N r_N} & \Gamma_{r_N \theta_N} \\ \Gamma_{\theta_N r_1} & \Gamma_{\theta_N \theta_1} & \cdots & \Gamma_{\theta_N r_N} & \Gamma_{\theta_N \theta_N} \end{bmatrix} \quad (16)$$

where $\Gamma_{pq} = E[\frac{\partial^2 \ln \mathcal{L}}{\partial p \partial q}]$, $\{p, q\} = \{r_1, \theta_1, r_2, \theta_2 \dots r_N, \theta_N\}$. The entries of FIM are [15]:

$$\Gamma_{pq} = \frac{2}{\sigma^2} \sum_{l=1}^L \text{Re}\{\mathbf{x}^H \mathbf{D}_p^H \mathbf{D}_q \mathbf{x}\}, \quad (17)$$

where $\mathbf{D}_p = \frac{\partial \mathbf{A}_{ms}}{\partial p}$ and $\mathbf{D}_q = \frac{\partial \mathbf{A}_{ms}}{\partial q}$. The columns of matrix \mathbf{A}_{ms} contain the scattered fields as defined in (1), and since the scattered fields are calculated using the recursive T-matrix algorithm, derivatives of \mathbf{A} with respect to object positions, \mathbf{D}_p and \mathbf{D}_q , can be easily obtained [23]. Since \mathbf{x} is constant over L experiments, (17) can be further reduced to:

$$\Gamma_{pq} = \frac{2L}{\sigma^2} \text{Re}\{\mathbf{x}^H \mathbf{D}_p^H \mathbf{D}_q \mathbf{x}\}. \quad (18)$$

The Cramér-Rao bound by definition is, then, the inverse of the FIM:

$$\text{CRB}(r_1, \theta_1, \dots, r_N, \theta_N) = J^{-1}. \quad (19)$$

The i th diagonal entry in the Cramér-Rao bound expression in (19) gives the Cramér-Rao lower bound for the i th variable in the parameter set $\{r_1, \theta_1, r_2, \theta_2 \dots r_N, \theta_N\}$. In Section 5, we will verify the analytical expressions given by (19) with the Monte-Carlo simulated error variances.

5 Examples

In this section, we present numerical examples on localization of multiple objects and verification of Cramér-Rao lower bounds with Monte-Carlo simulations. In order to simplify the scattering phenomenon associated with the detection problem, the targets are modeled as simple, circular objects with diameters of 7.5 cm. The system parameters are kept constant throughout the examples to allow meaningful comparisons. The scattered field due to an incident plane wave is observed

along a 33-element, uniform, linear receiver array which spans an aperture of 1.5 m. The sensors are assumed to be ideal, isotropic receivers. Unless otherwise noted, the operating frequency is set to 1.0 GHz. The objects are placed in a lossy, homogeneous background which has the same electrical characteristics of 5% moist San Antonio clay loam ($\epsilon_b = 6\epsilon_0$, $\sigma_b = 5 \times 10^{-2} \text{S/m}$) at around 1.0 GHz [21]. In all examples the scattering simulations are repeated 250 times to estimate the autocovariance matrices, i.e. $L = 250$ in (4) and (10).

In order to show the performance of the algorithms, we consider two objects geometries. In the first case (Fig. 3(a)), the objects are located quite far from each other. For this object geometry, due to the lossy background, the interactions between the targets are very weak. In the second case (Fig. 3(b)), the objects are located closely, and the electromagnetic interactions between the objects are considerably stronger.

For the simulations, the definition of signal to noise ratio (SNR) is not obvious. In practical problems, SNR is imposed by the nature of the system noise. However, in computer simulations we want to reference the noise power to a fixed quantity that does not change as the positions of the objects change. For this purpose SNR is referenced to the scattered field strength of a single, cylindrical, metallic object placed at the same depth as the objects, in the same lossy medium. The radius of the reference scatterer is the same as the radii of the targets. With this definition, the noise power is always proportional to the power of reference scattered field.

5.1 Multiple Object Localization: No Interaction

As described in Section 3.2, all scatterers are assumed to be scattering the incident plane wave independently. Therefore, we used the Mie series to generate the MUSIC spectrum in (8). The issue of signal coherence is solved by using two operating frequencies, 1.0 and 1.2 GHz. The autocovariance matrix at each frequency is estimated using (10), and the full rank autocovariance

matrix is calculated using (11). For a wide range of target locations, we have verified that the autocovariance matrix $\hat{\mathbf{R}}_d$ has two distinct signal eigenvalues that are quite different from the noise eigenvalues. The order of magnitude difference, of course, depends on the signal-to-noise ratio. At the 20 dB SNR level used in this example, the smallest signal eigenvalue is approximately two orders of magnitude larger than the largest noise eigenvalue.

In Fig. 4, we plot the MUSIC spectrum in (8) for the case of well separated objects. As the figure depicts, the target locations are indicated by two peaks that are easy to distinguish from the background. The spectrum for the closely packed object case is shown in Fig. 5. It is clear from the figure that the no-interaction approach fails for this case. This is expected, since the no interaction model ignores the multiscattering effects that are very strong for closely spaced scatterers.

Since ignoring electromagnetic interactions may result in estimation errors, or even prevent resolution of targets as in Fig. 5, we investigated the interaction between two extended objects and compared the results with filamentary objects. Consider a problem where two objects are located 15 cm below the array. The position of one is kept fixed at (125, -15) cm (i.e. about 1/4 of the way from the right edge of the array) while the second is moved from left to right such that the inter-object distance, d , varies from eight centimeters to one meter. The interaction term given by (12) for both extended objects (computed using the T matrix method) and the filamentary objects (obtained from (28)) are shown as a function of d in Fig. 6(a). It is clear from this figure that for both extended and infinitesimally thin objects, the interaction terms decay very similarly.

The link between estimation error and object separation is shown in Fig. 6(b). A comparison of Figs. 6(a) and (b) reveals the expected result that both estimation errors and interaction terms decay as the objects are located farther apart. Figs. 6(c) and (d) show the same comparisons in (a) and (b) when the objects are located 25 cm below the array, further indicating that the

simple interaction term of Appendix B clearly provides a good measure of the level of interaction between extended objects, and one may use this simple interaction criterion to decide whether the no-interaction case would result in acceptable estimation errors. In fact, we can use Figs. 6(a) and (b) to estimate how the no-interaction case would perform for geometries given in Fig. 3. When the objects are 1 meter apart, Fig. 6 indicates that the interaction term is insignificant, so is the estimation error. As seen from Fig. 4, for this case the object centers are clearly defined by two peaks around the true center coordinates. When the objects are separated by 10 cm, however, there is a considerable electromagnetic coupling between objects, and the estimation errors are so large that the objects centers cannot be resolved as verified in Fig. 5.

5.2 Multiple Object Localization: With Interaction

We have applied the algorithm given in Section 3.3 to localize the targets for the two geometries: well separated and closely spaced objects. The signal to noise ratio is fixed at 20 dB and the autocovariance matrix, and the projection operator onto the noise subspace is calculated.

To determine the positions of the two targets, we searched for the maximum of the spectrum $P_{MUSIC}(r_1, \theta_1, r_2, \theta_2)$ given by (13) in $(r_1, \theta_1, r_2, \theta_2)$ space. To find this maximum we use the steepest descend algorithm described in Section 3.3. Fig. 7 shows the intermediate object positions at each iteration during the multi-dimensional search. The objects are located 1 meter apart, and the initial guesses are denoted with *'s³. Large circles indicate the support of the objects. Although not clear from this figure, as the number of iterations increase, the location estimates get closer to the true estimates at (25, -15) and (125, -15) cm. Fig. 8 shows the object positions at each iteration during the multi-dimensional search when the objects are closely spaced. The

³Here we have initialized the search method by hand to illustrate the manner in which the search process functions. As described below, to verify the Cramer-Rao bound analysis, we employ an automatic method for initializing the nonlinear optimization.

distance between the targets for this case is 10 cm. Again the initial guesses are indicated with *'s, and as the number of iterations increase, the location estimates get closer to the true estimates at $(70, -15)$ and $(80, -15)$ cm. For both cases, we observed that this approach quickly converges to the general maximum area in 7-10 iterations using the steepest decent algorithm. After the initial quick convergence, we switch to a simplex search [22] to locate the precise maximum.

5.3 Verification of Cramér-Rao bounds

In this section, we will compare the analytical Cramér-Rao bound results obtained in Section 4 with the Monte-Carlo simulated error variances. For this purpose, the algorithms described in Sections 3.1 and 3.3 are repeated 500 times at different signal to noise ratios. For each Monte-Carlo simulation, the multi-dimensional search routine requires initial values for the positions of the targets. Thus, to supply the algorithm with an initial value, we used the subarray processing method described in [1]. This approach can efficiently provide rough estimates of the object locations. Once we initialize the object positions with subarray processing, we perform the multi-dimensional search described in the previous section. The position vector maximizing the spectrum is declared as the position estimates and the error variances are calculated from the estimates.

Fig. 9 shows the comparison of analytical CRB calculated for single object geometry of Fig. 2 using (19) with 500 Monte-Carlo simulations of the algorithm described in Section 3.1. The solid line is the CRB for the radial position of the object and measured in squared meters. The dashed line denotes the CRB for the angular position and measured in squared radians. The radial and angular positions are referenced to the center point of the array. Monte-Carlo simulated error variances for range and bearing variables are shown on the same plot with \circ and \diamond symbols, respectively.

Fig. 10 compares the Cramér-Rao bounds with simulated error variances for multiple object geometries of Fig. 3 using the algorithm of Section 3.3. Fig. 10(a) shows the comparison for two

objects located one meter from each other, and Fig. 10(b) show the comparison when the objects are 10 centimeters apart. Again, the solid and dashed lines are the CRBs for radial and angular positions of the objects, respectively. The range variables have the unit of squared meters, and the bearing variables have the unit of squared radians. As before, both coordinate variables are defined with respect to the center point of the array. The symbols \circ and \diamond show the Monte-Carlo simulated error variances for the range and bearing variables, respectively. For this case, since there are two targets present in the region, there are two symbols at each SNR value. The problem geometry is symmetric, thus, one would expect that the error variances should be the same. Indeed, for analytical Cramér-Rao bounds calculated from (19), the bounds for coordinates of both objects are the same. For the simulated error variances, however, we can notice the different values for the range variables in Fig. 10(a) and for the bearing variables in Fig. 10(b). The difference in simulated variances pronounced for low signal to noise ratios, which, we believe, implies that more Monte-Carlo simulations are needed at those SNR values.

In both Fig. 9 and Fig. 10, we observe that the simulated error variances approach the lower limit provided by the Cramér-Rao bounds as the signal to noise ratio increases. This is expected by the results reported in [15] which states that MUSIC is an efficient estimator for large SNR values. The results presented here, therefore, reveal that at high signal to noise ratios MUSIC is an efficient estimator for near field object localization problems, too.

6 Conclusions

In this paper we presented a matched field based high resolution array processing technique for localization of near field targets. The algorithm is presented in three parts: single object localization, multiple object localization ignoring the interactions between objects, and multiple object localization taking multiple scattering into account. When the interactions are ignored,

the computational load is alleviated since the electromagnetic model is a simple Mie series, and a two-dimensional search in parameter space suffices to localize all objects. The drawbacks, on the other hand, are the necessity to take care of the coherent signal issue, and the failure to resolve and localize closely spaced targets. When the electromagnetic interactions are accounted for, these drawbacks are remedied, but the computational load due to multi-dimensional search, and complex, multiple scattering forward model increases.

We have also calculated the analytical Cramér-Rao bound expressions for coordinates of multiple objects when the interactions are taken into consideration. These lower bounds are then verified with Monte-Carlo simulated error variances. We have shown that as the signal to noise ratio increases, simulated error variances approach the lower limit set by the Cramér-Rao bounds.

In terms of future work, our primary interest is the extension of this method to three dimensional buried objects for problems in which the halfspace between the air and the earth is explicitly modeled. This will require the generalization of the single object, half-space T matrix method of Kristensson and Stom [19] to the multi-object case as well as the development of MFP-type methods which are built around this new forward model.

Appendices

A Frequency Diversity

In this appendix, we will show that under simplifying assumptions the frequency diversity described by (10) and (11) increases the rank of the autocovariance matrix. Consider the data model $\mathbf{y}_i = \mathbf{s}_i + \mathbf{n}_i$ where \mathbf{s}_i is the noise-free scattered field due to a scatterer at frequency f_i , \mathbf{n}_i is the white, Gaussian noise as before, and \mathbf{y}_i is the observed data vector at frequency f_i , $i = 1, 2, \dots, N$. To simplify the problem, we will assume that the number of scatterers is limited

to two ($N = 2$), and the scatterers are infinitesimally thin.

The exact expression for the rank enhanced autocovariance matrix, \mathbf{R}_d is:

$$\mathbf{R}_d = \frac{1}{2} \mathbb{E} \{ \mathbf{y}_1 \mathbf{y}_1^H + \mathbf{y}_2 \mathbf{y}_2^H \} = \frac{1}{2} [\mathbf{s}_1 \mathbf{s}_1^H + \mathbf{s}_2 \mathbf{s}_2^H + 2\sigma^2 \mathbf{I}]. \quad (20)$$

For two scatterers, the frequency diversity should ensure that the signal subspace of \mathbf{R}_d is two dimensional. To see the conditions for which the signal subspace of \mathbf{R}_d is two dimensional, we rewrite (20) as:

$$\mathbf{R}_d = \underbrace{\frac{1}{2} [\mathbf{s}_1 \mathbf{s}_2] \begin{bmatrix} 1 & 0 \\ 0 & 1 \end{bmatrix} \begin{bmatrix} \mathbf{s}_1^H \\ \mathbf{s}_2^H \end{bmatrix}}_{\mathbf{S}} + \sigma^2 \mathbf{I}. \quad (21)$$

For the signal subspace of \mathbf{R}_d to be two dimensional, the matrix \mathbf{S} should have rank two which is possible if vectors \mathbf{s}_1 and \mathbf{s}_2 are linearly independent. Since the maximum likelihood estimate of the rank enhanced autocovariance matrix $\hat{\mathbf{R}}_d$ in (11) is asymptotically equal to \mathbf{R}_d , the proof for \mathbf{R}_d is valid for $\hat{\mathbf{R}}_d$ for large snapshots, i.e. $L \rightarrow \infty$. In the rest of the appendix, we show that \mathbf{R}_d has a two dimensional signal subspace, by proving that \mathbf{s}_1 and \mathbf{s}_2 are independent.

For this purpose, we show that the scattered fields due to the filament scatterers observed at two points, A and B , in space at two distinct frequencies, f_1 and f_2 , are independent. Thus, the data vectors measured over an array at more than two points will also be independent. The general Mie scattering series given in (9), is reduced to the following expressions for filament scatterers:

$$\begin{aligned} E_{s1}^A &= c_0 H_0^{(2)}(k_1 r_A) & E_{s2}^A &= d_0 H_0^{(2)}(k_1 r_A) \\ E_{s1}^B &= c_0 H_0^{(2)}(k_1 r_B) & E_{s2}^B &= d_0 H_0^{(2)}(k_2 r_B) \end{aligned} \quad (22)$$

where r_A and r_B denote the observation points, coefficients c_0 and d_0 are dependent on the frequency and object properties, $H_0^{(2)}(\cdot)$ is the zeroth order outgoing Hankel function, and k_i is the wavenumber at f_i , $i = 1, 2$. We will show that the vectors

$$\mathbf{s}_1 = \begin{bmatrix} E_{s1}^A \\ E_{s1}^B \end{bmatrix} \quad \text{and} \quad \mathbf{s}_2 = \begin{bmatrix} E_{s2}^A \\ E_{s2}^B \end{bmatrix} \quad (23)$$

are independent, i.e. equations

$$E_{s1}^A = \alpha E_{s2}^A \quad \text{and} \quad E_{s1}^B = \alpha E_{s2}^B \quad (24)$$

cannot be satisfied as long as $f_1 \neq f_2$.

Equations (22) and (24) imply that:

$$c_0 H_0^{(2)}(k_1 r_A) = \alpha d_0 H_0^{(2)}(k_2 r_A) \quad \text{and} \quad c_0 H_0^{(2)}(k_1 r_B) = \alpha d_0 H_0^{(2)}(k_2 r_B) \quad (25)$$

which can be written as

$$\gamma = \frac{\alpha d_0}{c_0} = \frac{H_0^{(2)}(k_1 r_A)}{H_0^{(2)}(k_2 r_A)} = \frac{H_0^{(2)}(k_1 r_B)}{H_0^{(2)}(k_2 r_B)}. \quad (26)$$

Properties of Hankel functions require that $|H_0^{(2)}(k_1 r)|$ and $|H_0^{(2)}(k_2 r)|$ are monotonically decreasing, and do not intersect at any r . These two properties and the fact that $H_0^{(2)}(k_1 r)/H_0^{(2)}(k_2 r)$ is not a constant imply that if we choose a γ such that $H_0^{(2)}(k_1 r_A) = \gamma H_0^{(2)}(k_2 r_A)$, then there would be no r_B which satisfies $H_0^{(2)}(k_1 r_B) = \gamma H_0^{(2)}(k_2 r_B)$ unless $k_1 = k_2$ and $\gamma = 1$. Therefore, the vectors in (23) are mutually dependent only when $k_1 = k_2$, i.e. $f_1 = f_2$.

B Bound on Electromagnetic Interactions

In this appendix, we derive the interaction terms between two infinitesimally thin scatterers. Using the definition of the interaction term in (12), we calculate the electromagnetic interactions between two infinitesimal scatterers here, and then compare these simple interaction terms with those of extended objects in Section 5.1.

First we derive the scattered field from two filamentary objects separated by a distance d , when they are excited with a plane wave, $e^{j\mathbf{k}\cdot\mathbf{r}}$. With a simple approach, schematically shown in Fig. 11, we account for the multiple scattering between these objects iteratively. The field scattered from the first object due to the plane wave is obtained by setting $n = 0$ in (9) and is $\mathbf{E}_{s1} = c_0 H_0^{(2)}(k|\mathbf{r}|)$ where c_0 depends on the object radius, and $|\mathbf{r}|$ is the distance between the scatterer and the receivers

in the array. Thus, the value of $\mathbf{E}_{\mathbf{s1}}$ at the location of the second object is $c_0 H_0^{(2)}(kd)$, where d is the distance between the two objects.

Still assuming no interaction, we use $c_0 H_0^{(2)}(kd)$ as incident field on the second object, and find the scattered field due to the wave scattered from the first object as: $\mathbf{E}_{\mathbf{s12}} = d_0 H_0^{(2)}(k|\mathbf{r}|)$ where $d_0 = c_0 [c_0 H_0^{(2)}(kd)]$. When this field arrives at the location of the first object, it becomes $d_0 H_0^{(2)}(kd)$. Using this as the incident field on the first object, we calculate the third term in our scattering series as $\mathbf{E}_{\mathbf{s121}} = e_0 H_0^{(2)}(k|\mathbf{r}|)$ with $e_0 = c_0 [d_0 H_0^{(2)}(kd)]$. By carrying no-interaction scattered fields between scatterers in this manner, the scattered field due to the first object, in the presence of the second is given in the form of an infinite sum:

$$\begin{aligned} \mathbf{E}_{\mathbf{s1}}^{(2)} &= \mathbf{E}_{\mathbf{s1}} + \mathbf{E}_{\mathbf{s12}} + \mathbf{E}_{\mathbf{s121}} + \mathbf{E}_{\mathbf{s1212}} + \dots \\ &= c_0 \left\{ 1 + c_0 H_0^{(2)}(kd) + [c_0 H_0^{(2)}(kd)]^2 + [c_0 H_0^{(2)}(kd)]^3 + \dots \right\} H_0^{(2)}(k|\mathbf{r}|). \end{aligned} \quad (27)$$

The difference between with-interaction and no-interaction fields can now be expressed as:

$$\mathbf{E}_{\mathbf{s1}}^{(2)} - \mathbf{E}_{\mathbf{s1}} = c_0 \{ c_0 H_0^{(2)}(kd) + [c_0 H_0^{(2)}(kd)]^2 + [c_0 H_0^{(2)}(kd)]^3 + \dots \} H_0^{(2)}(k|\mathbf{r}|),$$

which can be written concisely as:

$$\mathbf{E}_{\mathbf{s1}}^{(2)} - \mathbf{E}_{\mathbf{s1}} = \frac{c_0^2 H_0^{(2)}(kd)}{1 - c_0 H_0^{(2)}(kd)} H_0^{(2)}(k|\mathbf{r}|). \quad (28)$$

Expression in (28) is warranted since $|c_0 H_0^{(2)}(kd)| < 1$, where $c_0 = \frac{J_0(ka)}{H_0^{(2)}(ka)}$ and a is the radius of the object, $a < d$. Evaluation of (28) for \mathbf{r} equal to the positions of the receivers then provides the means of determining $\delta(d)$ in (12).

References

- [1] A. Şahin and E.L. Miller, "Object Detection Using High-Resolution Near-Field Array Processing", *IEEE Trans. on Geoscience and Remote Sensing*, Submitted for Review.
- [2] A. Şahin and E.L. Miller, "Object-Based Localization of Buried Objects Using High Resolution Array Processing Techniques", in *Proc. of SPIE- AeroSense: Detection and Remediation Technologies for Mines and Minelike Targets*, May 1996, vol. 2765, pp. 409–419.
- [3] A. Şahin and E.L. Miller, "Performance Bounds for Matched Field Processing in Subsurface

- Object Detection Applications”, in *Proc. of SPIE- AeroSense: Detection and Remediation Technologies for Mines and Minelike Targets III*, April 1998, vol. 3392.
- [4] H.Krim and M.Viberg, “Sensor Array Signal Processing: Two Decades Later”, Tech. Rep. CICS-P-448, Center for Intelligent Control Systems, January 1995.
 - [5] M. Bouvet and G. Bienvenu, Eds., *High-Resolution Methods in Underwater Acoustics*, Springer-Verlag, Heidelberg, Germany, 1991.
 - [6] A.B. Baggeroerr, W.A. Kupperman, and P.N. Mikhalevsky, “An Overview of Matched Field Methods in Ocean Acoustics”, *IEEE J. of Oceanic Engineering*, vol. 18, no. 4, pp. 401–424, October 1993.
 - [7] D.F. Gingras, P. Gerstoft, and N.L. Gerr, “Electromagnetic Matched-Field Processing: Basic Concepts and Tropospheric Simulations”, *IEEE Trans. on Antennas and Propagation*, vol. 45, no. 10, pp. 1536–1544, October 1997.
 - [8] J.W. Choi and Y.H. Kim, “Spherical Beam-Forming and MUSIC Methods for the Estimation of Location and Strength of Spherical Sound Sources”, *Mechanical Systems and Signal Processing*, vol. 9, no. 5, pp. 569–588, 1995.
 - [9] J.W. Choi and Y.H. Kim, “Estimation of Locations and Strengths of Broadband Planar and Spherical Noise Sources Using Coherent Signal Subspace”, *Journal of Acoustical Society of America*, vol. 98, no. 4, pp. 2082–2093, October 1995.
 - [10] Y.D. Huang and M. Barkat, “Near-Field Multiple Source Localization by Passive Sensor Array”, *IEEE Transactions on Antennas and Propagation*, vol. 39, no. 7, pp. 968–974, July 1991.
 - [11] N. Yuen and B. Friedlander, “Performance Analysis of Higher Order ESPRIT for Localization of Near-Field Sources”, *IEEE Transactions on Signal Processing*, vol. 46, no. 3, pp. 709–719, March 1998.
 - [12] D. Starer and A. Nehorai, “Passive Localization of Near-Field Sources by Path Following”, *IEEE Trans. Signal Processing*, vol. 42, no. 3, pp. 677–680, March 1994.
 - [13] N. V. Budko and P. M. van den Berg, “Two-Dimensional Object Characterization with an Effective Model”, *Journal of Electromagnetic Waves and Applications*, vol. 12, pp. 177–190, 1998.
 - [14] S. Valaee, B. Champagne, and P. Kabal, “Parametric Localization of Distributed Sources”, *IEEE Transactions on Signal Processing*, vol. 43, no. 9, pp. 2144–2153, September 1995.
 - [15] P. Stoica and A. Nehorai, “MUSIC, Maximum Likelihood, and Cramer-Rao Bound”, *IEEE Trans. Acoust., Speech, Signal Processing*, vol. 37, no. 5, pp. 720–741, May 1989.
 - [16] W.C. Chew, *Waves and Fields in Inhomogeneous Media*, Van Nostrand Reinhold, 1990.
 - [17] A. Şahin and E.L. Miller, “Recursive T-matrix Algorithm for Multiple Metallic Cylinders”, *Microwave Opt. Tech. Lett.*, vol. 15, no. 6, pp. 360–363, August 1997.

- [18] A. Şahin and E.L. Miller, “Recursive T-matrix Methods for Scattering from Multiple Dielectric and Metallic Objects”, *IEEE Trans. on Antennas and Propagation*, vol. 46, no. 5, pp. 672–678, May 1998.
- [19] G. Kristensson and S. Strom, “Scattering from buried inhomogeneities—a general three dimensional formalism”, *J. Acoust. Soc. Am.*, vol. 64, pp. 917–936, 1978.
- [20] J.A. Kong, *Electromagnetic Wave Theory*, John Wiley & Sons, 1986.
- [21] J.E. Hipp, “Soil Electromagnetic Parameters as Functions of Frequency, Soil Density, and Soil Moisture”, *Proceedings of the IEEE*, vol. 62, no. 1, pp. 98–103, January 1974.
- [22] W.H. Press, B.P. Flannery, S.A. Teukolsky, and W.T. Vetterling, *Numerical Recipes*, Cambridge University Press, Cambridge, UK, 1986.
- [23] Adnan Şahin, *Near Field Forward Scattering, and Object-Based Localization Algorithms for Subsurface Objects*, PhD thesis, Northeastern University, Boston, MA, 1998.

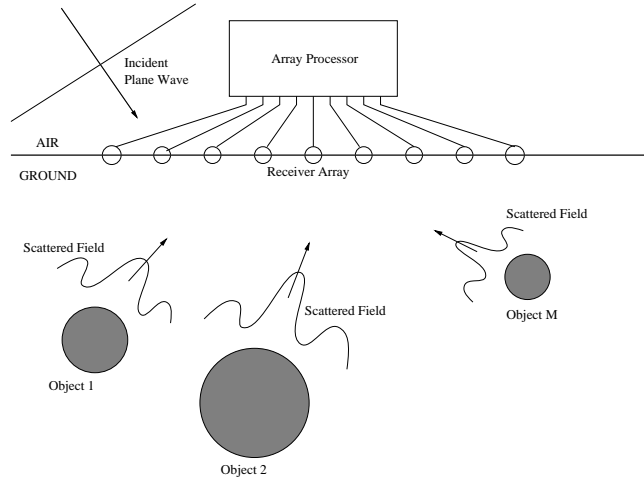


Figure 1: Problem geometry

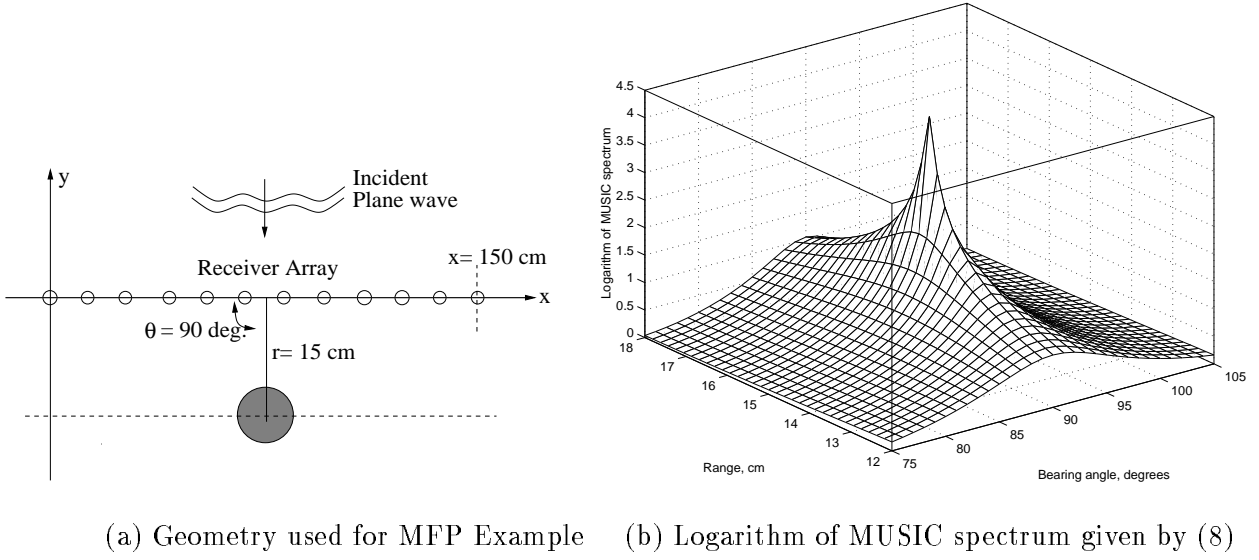


Figure 2: MFP localization example: single metallic object in a lossy, homogeneous background

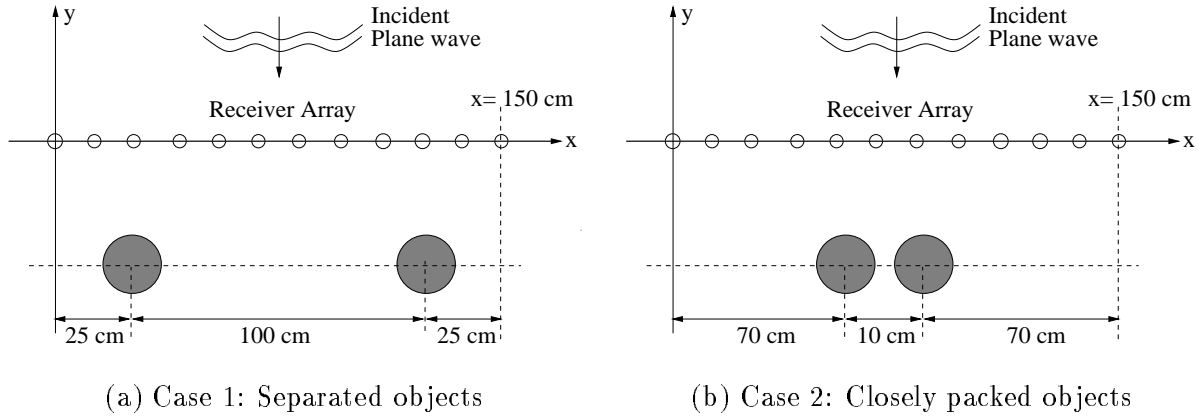


Figure 3: Example geometries used in multiple object localization

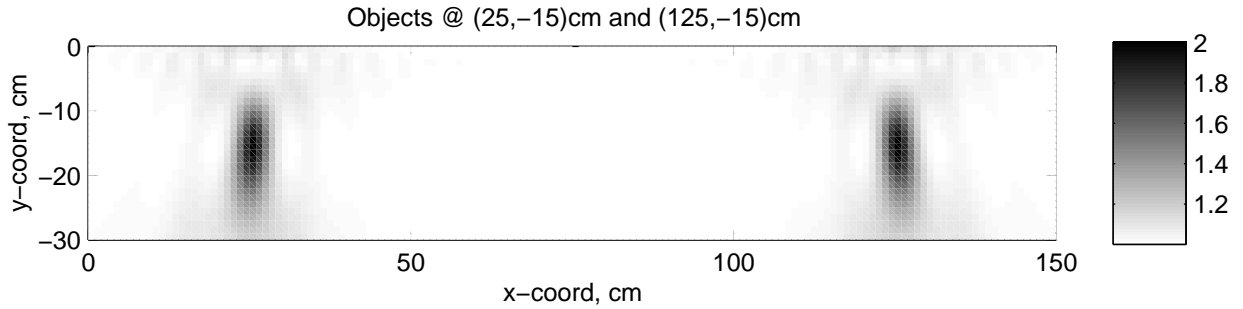


Figure 4: Localization of two targets located 1 meter apart, electromagnetic interactions are ignored

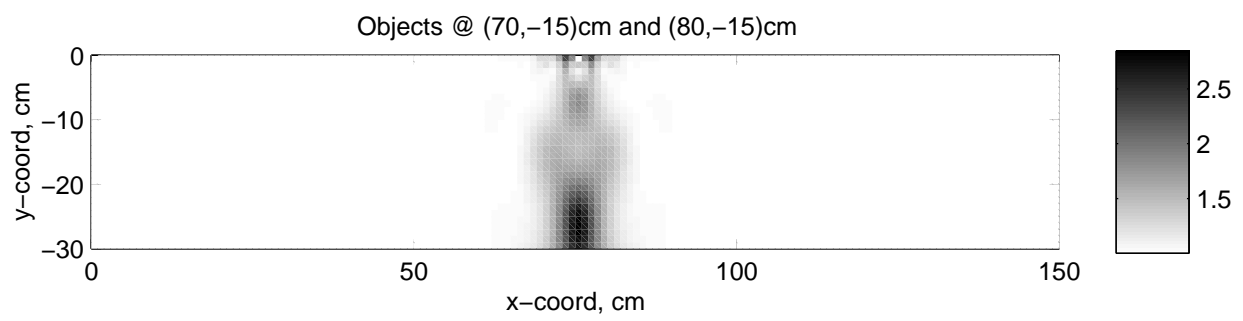
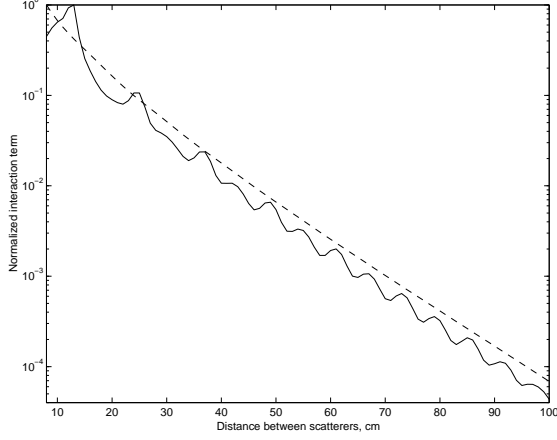
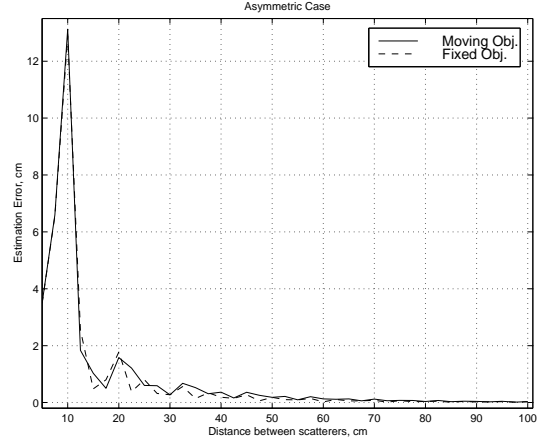


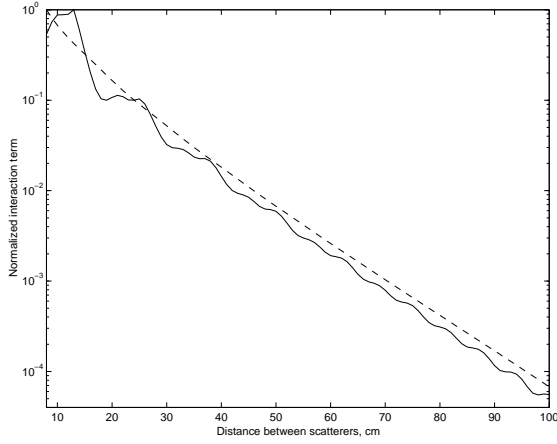
Figure 5: Localization fails when the target centers are 10cm apart in the no interaction case



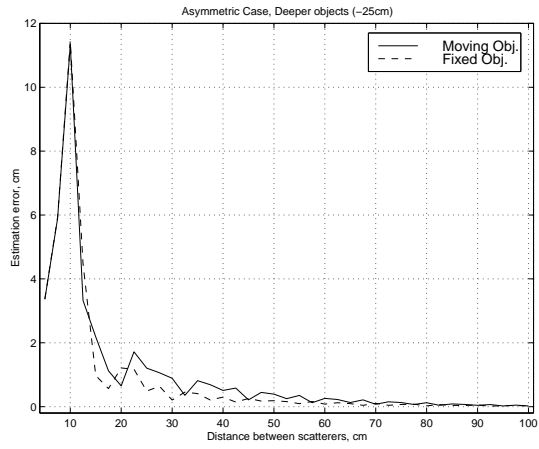
(a) Comparison of normalized interaction terms; solid line extended objects, dashed line filament objects, objects 15 cm away from the array



(b) Estimation error vs. separation for no interaction case, objects 15 cm away from the array

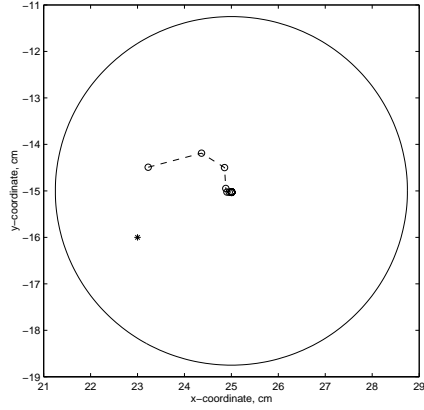


(c) Same as (a), objects 25 cm away from the array

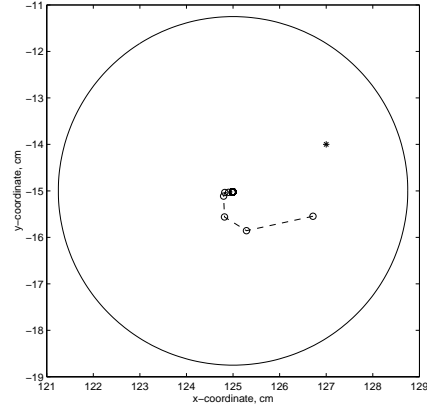


(d) Same as (b), objects 25 cm away from the array

Figure 6: Electromagnetic interaction between scatterers, and its effect on estimated object coordinates when the objects are 15 cm away from the receiver array (top plots) and 25 cm away (bottom plots)



(a) Object @ (25,-15)cm



(b) Object @ (125,-15)cm

Figure 7: Convergence of four-dimensional search into the true object coordinates when the objects are 1 meter apart, *'s indicate the initial guess, and the large circle indicates the support of the objects

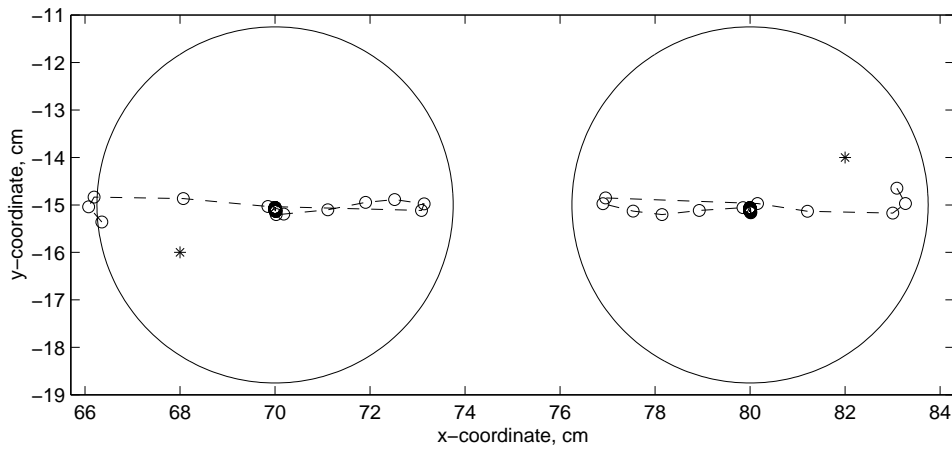


Figure 8: Convergence of four-dimensional search into the true object coordinates when the objects are 10 cm apart. *'s indicate the initial guess, and large circles indicate the support of the objects

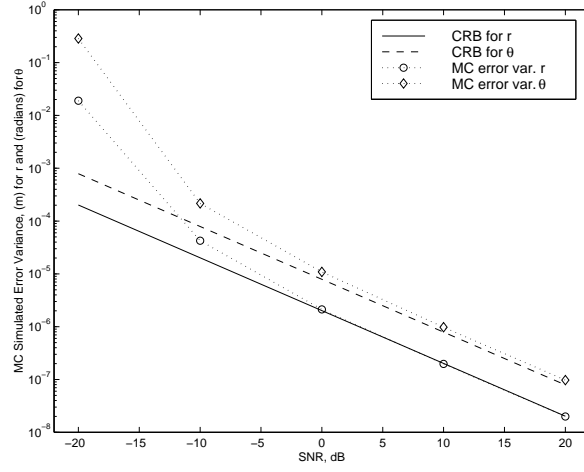
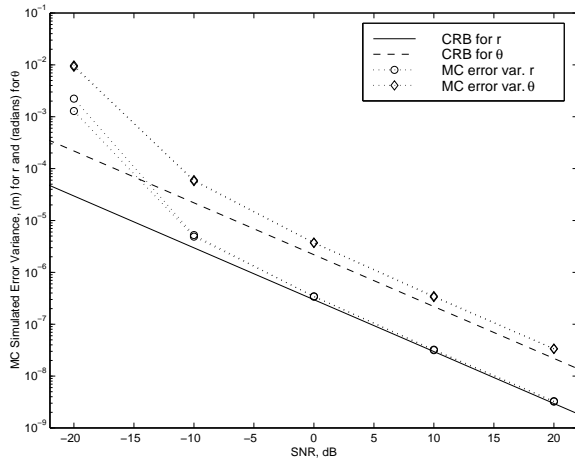
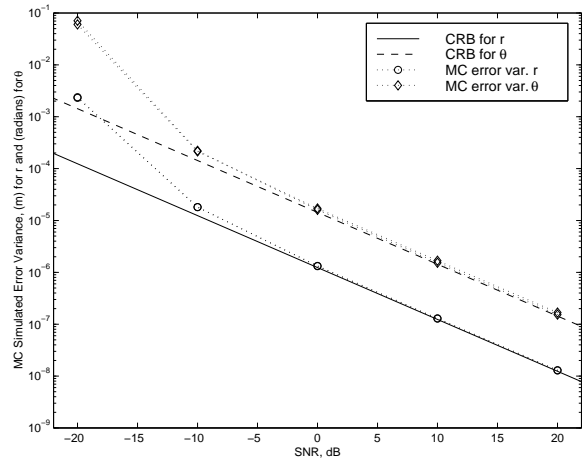


Figure 9: Comparison of analytical CRB with Monte-Carlo simulations for single object geometry given in Fig 2(a)



(a) Well separated objects, Fig 3(a)



(b) Closely spaced objects, Fig 3(b)

Figure 10: Comparison of analytical CRB with Monte-Carlo simulations for multiple object geometries given in Fig. 3

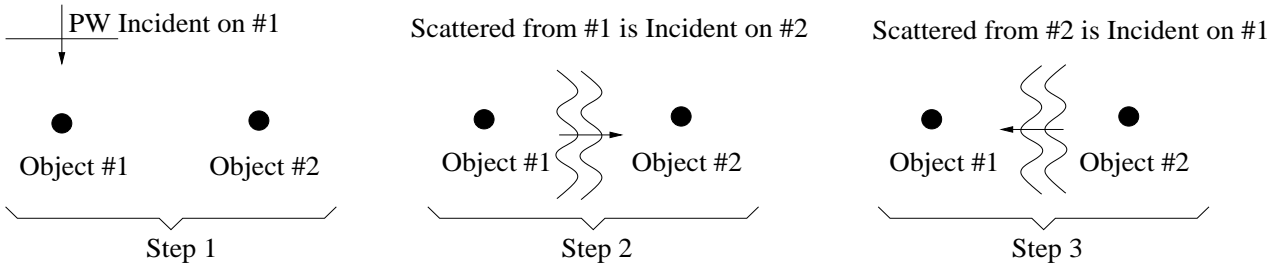


Figure 11: Finding the scattered field due to a filamentary object by incorporating the electromagnetic interactions between two scatterers step by step. Steps 2 and 3 are repeated infinitely many times successively to account for all interactions